Eur. Phys. J. D **42**, 189–196 (2007)
DOI: 10.1140/epjd/e2007-00020-2

THE EUROPEAN PHYSICAL JOURNAL D

Electron flux distributions in photodetachment of H^- in parallel electric and magnetic fields

S. Gao[1], G.C. Yang[2], S.L. Lin[1,a], and M.L. Du[3]

[1] College of Physics and Electronics, Shandong Normal University, Jinan 250014, P.R. China
[2] School of Physics and Electronic Information, Wenzhou University, Wenzhou 325027, P.R. China
[3] Institute of Theoretical Physics, Chinese Academy of Sciences, Beijing 100080, P.R. China

Received 11 April 2006 / Received in final form 30 November 2006
Published online 31 January 2007 –

Abstract. Photo-detached electrons of negative hydrogen ion in parallel electric and magnetic fields show quite complicated classical dynamical behavior, and a sequence of bifurcation and anti-bifurcation occurs. We investigate the effects of bifurcations on the flux distribution of photo-detached electrons by using position and momentum diagrams. Detached-electron flux distributions are calculated based on a uniform semi-classical theory. The flux distributions exhibit patterns with multiple rings. The bright rings correspond to special points in the diagrams. The flux distributions can be controlled by adjusting the magnetic field strength while fixing the electric field.

PACS. 32.80.Fb Photoionization of atoms and ions – 03.65.Sq Semiclassical theories and applications

1 Introduction

With the development of photodetachment microscope technology it is possible to observe the spatial distributions of detached-electron on a screen. The spatial distributions provide information about the negative ion wave function before detachment. Blondel's group completed the first such experiment for Br^- ions in a homogeneous electric field [1]. Inspired by this pioneer work, studies have been extended to other ions, atoms and molecules [2–5]. Since the detached-electron flux distribution is sensitive to parameters such as photon energy, the binding energy of negative ion and the strengths of external fields, it has been used to obtain binding energies of negative ions with high precision [5].

Theoretical investigations on the photodetachment microscope of negative ions in a static electric field were described using semi-classical and other methods [6,7]. The photo-detached electron distribution on a screen perpendicular to the field shows a concentric structure resulting from the interference of two distinctive electron paths. Oscillations in the total photodetachment cross section in parallel electric field and magnetic fields have been predicted more than ten years ago, but the experiment was carried out recently [8]. However, measurements on spatial distributions of detached-electrons in parallel electric and magnetic fields using photodetachment microscope are still not yet available. Recently several interesting articles have appeared addressing the theoretical questions of detached-electron distribution in parallel fields [9–12]. A point source was used to simulate the initial detached-electron in all these works. Usually an isotropic point like source was used [9–11]. The results using such a source should be useful for photo-detachment from a negative ion in a p-wave state very near detachment threshold where the d component of the detached electron can be neglected compared to the s component. However, the results cannot be directly applied to the photo-detachment of H^- in parallel electric and magnetic fields because H^- is in an s-wave state and the detached-electron is a p-wave. The initial detached outgoing wave is important in determining the images on the screen. A point like multipole source was introduced and applied only to study the p-wave photodetachment in an electric field [12].

This article is about the photodetachment of H^- in parallel electric and magnetic fields. We take the specific initial wavefunction of H^- into consideration and describe the resulting angular dependent detached-electron wavefunction (a p-wave). We pay particular attention to the ring patterns in the flux distributions on the screen, and we show these patterns can be modified by external fields. A semiclassical method is used since it gives quite intuitive physical pictures. The method is easy to apply numerically. A different method based on catastrophic theory was used to deal with singularities in references [9–11].

[a] e-mail: sllin@sdnu.edu.cn

Semiclassical theory has achieved great success in studying photo-absorption properties of atom, negative ion and molecule in applied strong external fields since it was proposed [13–16]. The divergence in the wave function associated with the bifurcation of classical orbit [17–19] can be fixed by using a mixed position and momentum representation of semiclassical wave function [20]. We will calculate the detached-electron flux distribution images on the screen using the mixed position and momentum representation for the detached-electron. We will show the major features of the detached-electron images are rings, which can be controlled by adjusting the magnetic field. What makes the current system more interesting is that the classical orbits of the photo-detached electrons bifurcate with the external parameters such as the photon energy and the magnetic field strength. The relationship between the ring patterns in the detached-electron images and the bifurcation of classical orbits is discussed using $\rho - p_\rho$ diagrams.

This paper is organized as follows. In Section 2, we describe the system, the electron's classical motion and the bifurcation of classical orbits using $\rho - p_\rho$ diagrams. In Section 3, a uniform semiclassical method in a mixed position and momentum representation is described and used to propagate the detached-electron wave function from the negative ion to the screen perpendicular to the fields. We then calculate and display the images of detached-electron flux distributions on the screen. We also discuss the correspondence between the structures in the images and the bifurcation or anti-bifurcation. A short conclusion is given in Section 4. Atomic units are used throughout unless otherwise noted.

2 Classical motion and bifurcation

To investigate the flux of photo-detached electrons of H^- in parallel electric and magnetic fields in semiclassical framework, we have to find all emanating trajectories of the active electron from the atomic core. Take the direction of the electric and magnetic fields as the z-axis and use the cylindrical coordinates (ρ, z, ϕ). A Hydrogen negative ion H^- sits at the origin and a z-polarized laser is applied. H^- can be regarded as a one-electron system with an active electron loosely bound by a short-range spherical symmetric potential. In cylindrical coordinates (ρ, z, ϕ), the Hamiltonian governing the electron motion after photodetachment is [17]

$$H = \frac{1}{2}\left(p_\rho^2 + \frac{L_z^2}{\rho^2}\right) + \omega_l L_z + \frac{1}{2}\omega_l^2\rho^2 + \frac{1}{2}p_z^2 + Fz + V_p(r) \quad (1)$$

where ω_l is the Larmor frequency, $\omega_l = \mathbf{B}/2c$, F and B are the electric and magnetic field strengths, respectively, $V_p(r)$ is a short-range potential, where r is the distance between the active electron and the nucleus [21], and L_z is the z-component of the angular momentum, which is a constant of motion. It is a good approximation to neglect $V_p(r)$.

The electron motion can be separated into two parts: the motion along the z-axis is a uniform acceleration, and the motion in the $x-y$ plane is a circular cyclotron motion. Take the angle of the initial outgoing direction and the z-axis to be θ_0, the trajectory of the detached-electron in cylindrical coordinates is given by

$$\begin{cases} \rho = k\sin\theta_0 \left|\sin(\omega_l t)\right| / \omega_l \\ z = -t^2 F/2 + kt\cos\theta_0 \end{cases} \quad (2)$$

and the corresponding momentum is

$$\begin{cases} p_\rho = k\sin\theta_0\cos(\omega_l t) \\ p_z = -Ft + k\cos\theta_0 \end{cases} . \quad (3)$$

The time t_f for a detached-electron to reach the screen perpendicular to the z-axis at $z < 0$ is

$$t_f = \left(k\cos\theta_0 + \sqrt{k^2\cos^2\theta_0 - 2Fz}\right)/F. \quad (4)$$

The maximum and the minimum of t_f are

$$t_{max} = \left(k + \sqrt{k^2 - 2Fz}\right)/F, \quad (5)$$

$$t_{min} = \left(\sqrt{k^2 - 2Fz} - k\right)/F. \quad (6)$$

They correspond to the initial angle $\theta_0 = 0$ and π.

The ρ motion is the same as the cyclotron motion in the magnetic field. The cyclotron period is

$$t_c = \pi/\omega_l. \quad (7)$$

When $t_f = nt_c$ (n is a positive integer), the detached-electron collides with the z-axis.

The behaviors of the detached-electron in coordinate space are rather complicated [9–11,17]. Here we analyze the detached-electron dynamics using $\rho - p_\rho$ diagram. By substituting time in equation (4) into ρ in equation (2) and p_ρ in equation (3), the curve parameterized by angle θ_0 from 0 to π is the $\rho - p_\rho$ diagram. A $\rho - p_\rho$ diagram is in a way similar to a surface of section. The diagram will be useful in understanding the structures in the detached-electron images on the screen. In the following calculations, the energy of the electron is 0.01 a.u., the electric field is 100 V/cm, and the screen is at $z = -5 \times 10^6$ a.u. The $\rho - p_\rho$ diagrams at various magnetic fields are drawn in Figure 1. For clarity the value of ρ can be negative. The solid lines stand for the orbits with initial angle $\theta_0 \le \pi/2$, and the dash lines stand for the orbits with $\theta_0 > \pi/2$. The solid lines and the dash lines join smoothly. In Figure 1a, the magnetic field is very small, the $\rho - p_\rho$ diagram is almost identical to the one with only an electric field [7]. ρ_c is a boundary, it divides the whole range for ρ into a classically allowed region and a classically forbidden region. For every ρ in $(0, \rho_C)$, there are two p_ρ, consequently there are also two orbits reaching the same point ρ on the screen; for ρ larger than ρ_C, there are no classical orbits.

As the magnetic field is increased, the cyclotron period decreases. Figures 1b–1j are $\rho - p_\rho$ diagrams with increasing magnetic field. In Figure 1b, when the magnetic field

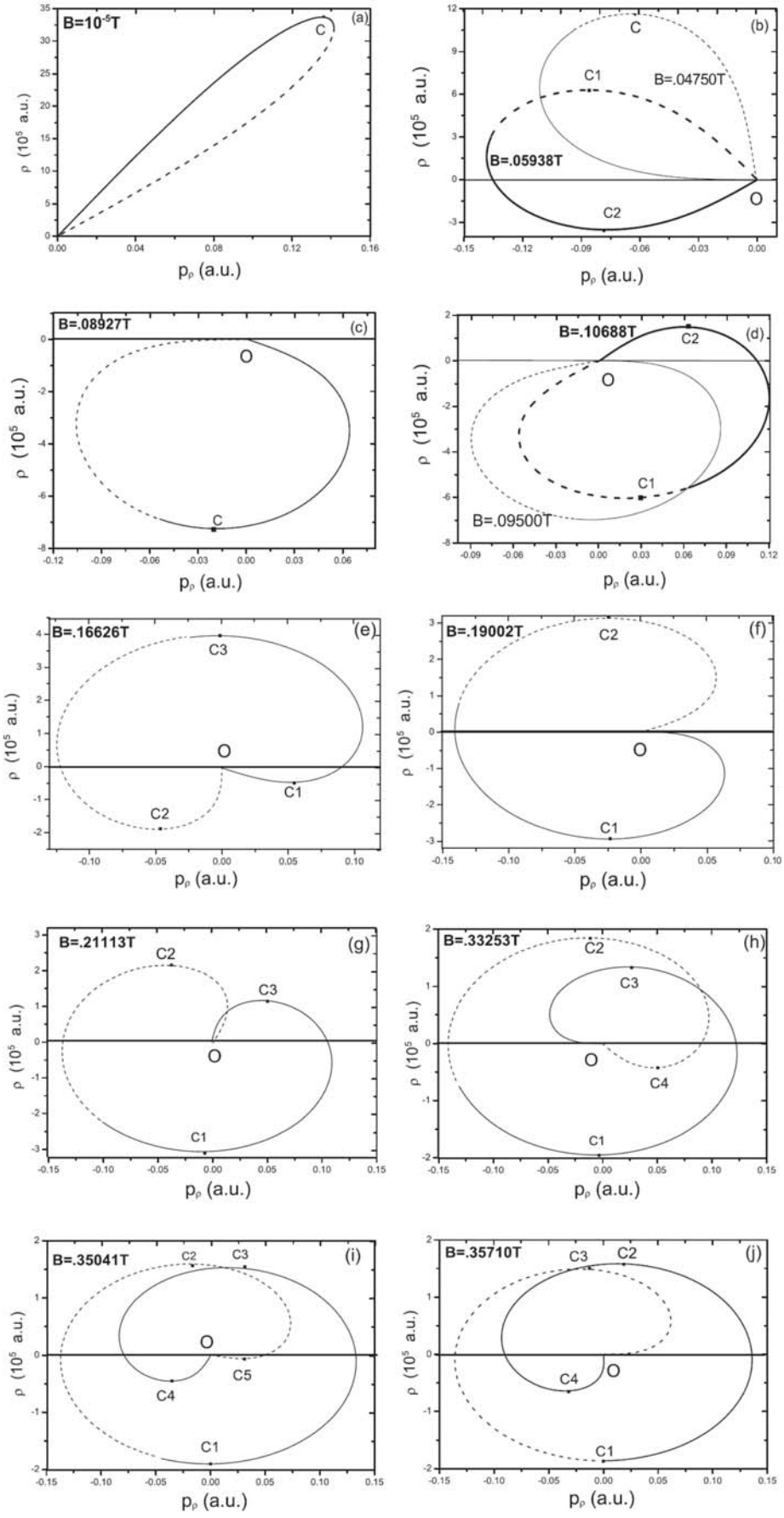

Fig. 1. The $\rho - p_\rho$ diagrams of detached-electron calculated on a screen at $z = -5 \times 10^6$ a.u. for various magnetic fields. The detached-electron energy $E = 0.27$ eV and the electric field $F = 100$ V/cm. The solid lines are for the orbits with initial angle $\theta_0 \leq \pi/2$, and the dash lines are for $\theta_0 > \pi/2$. ρ is extended to negative in the diagrams for clarity. The number of intersection points between a $\rho - p_\rho$ curve and a line defined by $|\rho| =$ constant gives the number of orbits arriving at the same point ρ on the screen. C_i are the boundary points. The thin lines in (b) and (d) correspond to magnetic field $B = B_b$ and $2B_b$, respectively. In (f) $B = 4B_b$, in (h) $B = 7B_b$, and in (j) $B = 4B_d$.

is 0.04750 T, the flight time of the orbit along the z-axis is equal to the cyclotron period, $t_{max} = t_c$, then the tangent of the solid line at O coincides with the p_ρ-axis as shown by the thin curve in Figure 1b. If the magnetic field is increased slightly, the solid line will move across the p_ρ-axis as shown by the thick curve in Figure 1b for a magnetic field 0.05938 T. Fold caustics are formed near the special boundary points C_1 and C_2 for the thick curve in Figure 1b. For any point satisfying $0 < |\rho| < |\rho_{C2}|$, there are four values of p_ρ corresponding to the same ρ. There are also four detached-electron orbits reaching the same point on the screen in this range. For $|\rho_{C2}| < |\rho| < |\rho_{C1}|$, there are two values for p_ρ corresponding to the same ρ, there are two detached electron orbits reaching the same point on the screen in this range. Figure 1b shows a bifurcation when the magnetic field is increased just above 0.04750 T, then ρ_{C2} increases from zero to a small but finite value and the number of orbits increases by two. We call the magnetic field corresponding to $t_{max} = t_c$ the first bifurcation magnetic field B_b. Combining equations (5) and (7) gives

$$B_b = (2\pi cF)/\left(k + \sqrt{k^2 - 2Fz}\right). \tag{8}$$

B_b is equal to 0.04750 T in our case.

Figure 1c shows the disappearance of two orbits as the magnetic field is increased from below B_d to above B_d. B_d is calculated by setting $t_{min} = t_c$ and is given by

$$B_d = (2\pi cF)/\left(\sqrt{k^2 - 2Fz} - k\right). \tag{9}$$

When B is close to but smaller than B_d, the $\rho - p_\rho$ diagram is similar to the thick line in Figure 1b except ρ_{C1} is small. In this case, there are four orbits for small ρ but two orbits for larger ρ. When $B = B_d$, the tangent of dash lines at O coincides with p_ρ-axis as shown in Figure 1c, the entire curve is below the p_ρ-axis. Now only two orbits can reach the same point on the screen in the whole classically allowed region. Two orbits have disappeared near z-axis as the magnetic field is increased from below B_d to above B_d. We call the magnetic field B_d the first anti-bifurcation magnetic field. Its value is 0.08927 T in our system.

As the magnetic field is increased further above B_d, the number of orbits remains two until the magnetic field is twice of B_b, or $B = 0.09500$ T, then the tangent of the solid line of the diagram at O coincides with p_ρ-axis again as shown by the thin line in Figure 1d. If the magnetic field is increased slightly above 0.09500 T, part of the curve will be above the p_ρ-axis, the number of orbits will be four in the small ρ region. New orbits are created again. Similar phenomena happen for larger magnetic field. For example, Figures 1f and 1g show the diagrams at $B = 4B_b$ and above it; Figures 1h and 1i show the diagrams at $B = 7B_b$ and above it; Figure 1j shows the diagram at $B = 4B_d$. When the magnetic field is n times of B_b, we have $t_{max} = nt_c$, two new orbits will come into play near z-axis. When B is slight above mB_d, we have $t_{min} = mt_c$, two orbits will disappear. Therefore, for a given magnetic field B, the largest number of orbits reaching the same point of the screen can be determined using

$$N_{max} = 2 + 2(m^* - n^*) \tag{10}$$

where m^* and n^* are integers $(m^*, n^* = 0, 1, 2, ...)$ and determined from $m^*B_b < B < (m^* + 1)B_b$ and $n^*B_d < B < (n^* + 1)B_d$.

3 Detached-electron wavefunction and electronic flux distributions

For a photodetachment microscope, a screen away from the negative ion is used to detect the detached-electron flux. Assuming the screen perpendicular to the z-axis intersecting the axis at $z < 0$. The electron flux distribution on this screen can be calculated using [6,7]:

$$\frac{d^2\sigma(\rho, z, \varphi)}{\rho d\rho d\varphi} = -\frac{2\pi(E_b + E)}{c}\mathbf{j} \cdot \mathbf{k} \tag{11}$$

where

$$\mathbf{j} = \frac{i}{2}\left(\psi_f \nabla\psi_f^* - \psi_f^* \nabla\psi_f\right), \tag{12}$$

ψ_f is the detached-electron wavefunction satisfying an inhomogeneous equation, and $\mathbf{k}$ is a unit vector normal to the screen. We calculate the wavefunction by using semi-classical method. Imagine a sphere with radius r_0 ($5a_0 \leq r_0 \leq 100a_0$) enclosing the hydrogen negative ion which divides the space into two regions. Inside the sphere, the external fields can be neglected, and outside the sphere, the short range potential can be neglected. Because the initial state of H^- is an s-state, when a laser polarized in the z-direction is applied, a p-wave detached-electron is produced due to selection rules. The non-isotropic outgoing wave function is given by [6]

$$\psi_{out}(r) = \psi_{out}(\rho, z) = U(k)\frac{ke^{ikr}}{r}\cos\theta \tag{13}$$

where $U(k) = -4iB_0/(k_b^2 + k^2)^2$ and $E_b = k_b^2/2$ is the binding energy. This outgoing wave is continued with semi-classical method from the surface of the small sphere to large r, which is described by classical trajectories [13,14],

$$\psi_f(\mathbf{r}) = \sum_{j=1}^{n} \psi_{out}(\mathbf{r}_0) A_j(\mathbf{r}) \exp\left[i\left(S_j(\mathbf{r}) - \mu_j\pi/2\right)\right] \tag{14}$$

n counts the number of the trajectories that arrive at the final point. $A_j(\mathbf{r})$ is the amplitude, it represents the divergence of adjacent trajectories in time. $S_j(\mathbf{r})$ is the classical action of the jth orbit, and μ_j is the Maslov index.

The wavefunction in equation (14) diverges at singular points. A uniform approximation can be obtained by using mixed position and momentum representation [7,20]. Since the present system has cylindrical symmetry, the dynamics is reduced to a two-dimensional system. The orbits can be described in a 4-dimensional phase space using coordinates (p_ρ, p_z, ρ, z). It is convenient to use the mixed position and momentum variables (p_ρ, z) for this problem [7].

The initial outgoing wave function in the mixed position and momentum variables is obtained from the Fourier transform

$$\tilde{\psi}_{out}(p_\rho, z) = (2\pi i)^{-1/2} \int \psi_{out}(\rho, z) \exp(-i\rho p_\rho) d\rho. \quad (15)$$

The integral can be carried out using stationary-phase approximation. Let $\Phi = \vec{k} \cdot \vec{r} - \rho p_\rho$, the stationary point satisfies $\partial\Phi/\partial\rho = 0$. The result of the integral is

$$\tilde{\psi}_{out}(p_\rho, z) = U(k)\sqrt{\frac{k}{r_0}} \exp(ik_z z_0). \quad (16)$$

As in the configuration space, the wavefunction in (p_ρ, z) space can be propagated

$$\tilde{\psi}(p_\rho, z) = \sum_{i=1}^{n} \tilde{\psi}^i_{out}(p_\rho, z) \tilde{A}^i(p_\rho, z) \exp i \left[\tilde{S}^i(p_\rho, z) - \frac{\pi}{2}\nu^i\right]. \quad (17)$$

The summation runs over all trajectories which arrive at the same point (p_ρ, z), and $\tilde{A}^j$ is the corresponding amplitude [7]

$$\tilde{A} = \sqrt{\frac{\rho(t=0)}{\rho(t)}} \sqrt{\frac{\tilde{J}(t=0,\theta)}{\tilde{J}(t,\theta)}} \quad (18)$$

$$\tilde{J}(t,\theta) = \frac{\partial(p_\rho, z)}{\partial(t,\theta)}. \quad (19)$$

The classical action in the mixed position and momentum variables (p_ρ, z) will be denoted by $\tilde{S}(p_\rho, z) = \int p_z dz - \int \rho d\, p_\rho$. It is related to the action in coordinate space $S(\rho, z)$ by

$$\tilde{S}(p_\rho, z) = S(\rho, z) - \rho p_\rho. \quad (20)$$

The uniform approximation for the detached-electron wave function on the screen is obtained from

$$\psi_f(\rho, z) = \frac{i}{2\pi} \int \sum_{i=1}^{n} \tilde{\psi}^i_{out}(p_\rho, z) \tilde{A}^i(p_\rho, z) \times \exp i \left[\tilde{S}^i(p_\rho, z) - \frac{\pi}{2}\nu^i + p_\rho \rho\right] dp_\rho. \quad (21)$$

Away from singular points, the above integral can be carried out using stationary-phase approximation, and the result is the same as the one obtained via direct propagation in coordinate space. The phase of equation (21) is

$$\Phi_i = p_\rho \rho + \tilde{S}^i(p_\rho, z) - \nu^i \pi/2. \quad (22)$$

The stationary-phase points are determined by $\partial\Phi_i/\partial p_\rho = \rho - \rho_i(p_\rho, z) = 0$ and $\partial^2\Phi_i/\partial p_\rho^2 \neq 0$. $\rho_i(p_\rho, z)$ are the intersection points of the diagrams in Figure 1 with straight horizontal lines. When $\rho_i(p_\rho, z)$ are well separated from the extreme point such as ρ_{C2}, the stationary-phase approximation for the integral in equation (21) can be used. Near singular points, we expand the phase part in equation (21) to the third order and use the Airy approximation as done before when only an electric field is present [7]. Define $A(\rho, z) = \tilde{\psi}^i_{out}(p_\rho, z)\tilde{A}^i(p_\rho, z)$, and $B(z) = (-\partial^3\Phi_i/\partial p_\rho^3)^{1/3}\big|_{p_\rho = p_\rho^{ci}}$, the wavefunction in coordinate space is

$$\psi_f(\rho, z) = 2\pi^{1/2} A(\rho, z) B(z) Ai\left[-B(z)(\rho - \rho_{ci})\right] \times \exp\left[i\left(\Phi(z, p_\rho^{ci}) - \frac{\pi}{4}\right)\right]. \quad (23)$$

We now calculate the detached-electron wavefunctions and the detached-electron flux distributions on the screen using the method described above. We will increase the magnetic field while keeping the electron's energy and the electric field fixed. We take the same parameters as in Figure 1. The results for the detached-electron flux distributions as a function of ρ are shown in Figure 2. Because it is classically forbidden for large ρ, the electron flux vanishes there. As ρ is decreased, the flux distributions become more oscillatory. The flux distributions are divided into intervals by the special points in the diagrams in Figure 1 such as C, C_1 and C_2. For example, when the magnetic field $B = B_b$ as in Figure 2a, the flux is an interference of two orbits. The point C in Figure 2a is the point C in Figure 1b. When the magnetic field is 0.05938 T corresponding to the thick line in Figure 1b, $|\rho_{C1}| = 6.29 \times 10^5$ a.u. and $|\rho_{C2}| = 3.52 \times 10^5$ a.u., four orbits interfere in the region $\rho < |\rho_{C2}|$. When ρ is exactly at $|\rho_{C2}|$, two of the orbits degenerate into one, there are three orbits. Only two orbits interfere in the region $|\rho_{C2}| < \rho < |\rho_{C1}|$. When ρ is equal to $|\rho_{C1}|$, the remaining two orbits degenerate into one orbit. $\rho > |\rho_{C1}|$ is the classical forbidden region, there is no orbit. The details of interference near C_2 are shown in the inserts. When the magnetic field is increased to $B = 0.08927$ T, the structure in the $\rho - p_\rho$ diagram is simple again, the special points C_1 and C_2 no longer exist, there are only two orbits in the classical allowed region $\rho < |\rho_C|$, the corresponding flux distribution is shown in Figure 2c, which is quite similar to Figure 2a where the magnetic field can be neglected. The correspondence between the $\rho - p_\rho$ diagrams in Figure 1 and the detached-electron flux distributions in Figure 2 can be discussed similarly for larger magnetic field cases. For example, when $B = 0.21113$ T, there are three special points C_1, C_2 and C_3 in Figure 1g, these three points are identified in the corresponding flux distribution shown in Figure 2e. When $B = 0.35710$ T, the four special points in Figure 1j have important impacts in the detached-electron flux distribution in Figure 2f. In all cases, we found the $\rho - p_\rho$ diagrams are useful to understand the detached-electron flux distributions.

In Figure 3, we show the electron flux distribution close to C_2 labeled by an arrow in Figure 2b. The thin line stands for the flux distribution calculated using the semiclassical wavefunction in coordinate space. It diverges as expected. The thick line is the uniform result obtained using the mixed position and momentum variables (p_ρ, z). As ρ decreases across the boundary point C_2, the orbits reaching the screen increase from 2 to 4. The two new orbits coalesce at C_2. We found the wave amplitudes associated with the two new orbits are larger. The broad

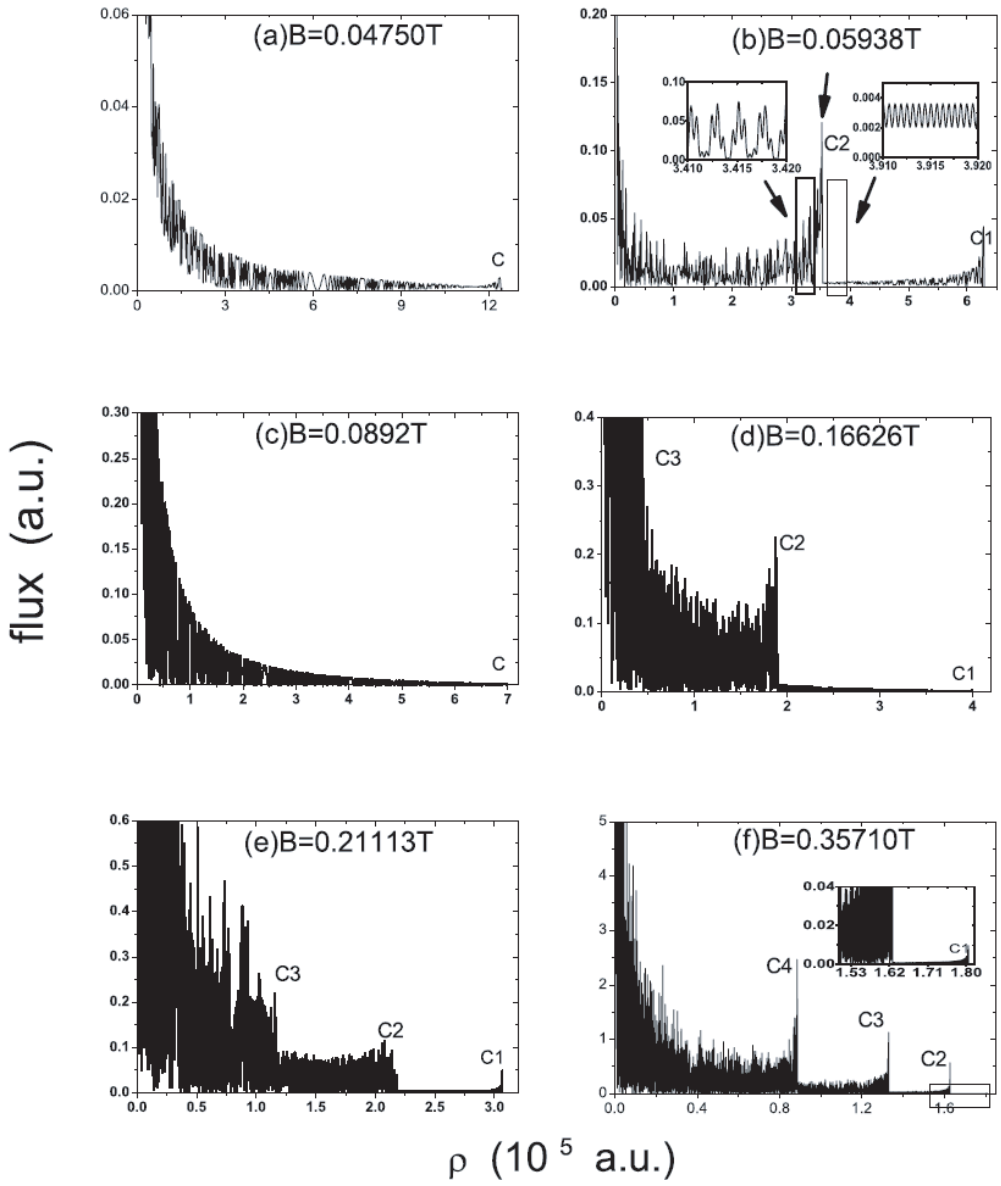

Fig. 2. Detached-electron flux distributions as a function of ρ at different magnetic fields. Detached-electron energy $E = 0.27$ eV, static electric field $F = 100$ V/cm, and the screen is at $z = -5 \times 10^6$ a.u. The inserts show the details of the interference. The points C, C_1 and C_2 are the special points in the $\rho - p_\rho$ diagrams in Figure 1.

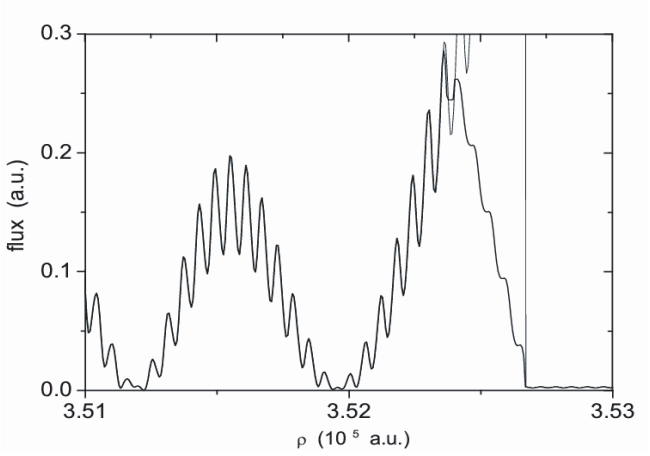

Fig. 3. Detached-electron flux distribution near C_2 calculated using a uniform semi-classical wavefunction (thick line) and a primitive semi-classical wavefunction (thin line).

fringes with almost 100% contrast come from the interference of the waves associated with the two new orbits, while the narrow fringes with a lower contrast are due to the two orbits existing on both the left and right of C_2.

In Figure 4 we show the detached-electron images corresponding to magnetic field B equal to 0.04750 T, 0.05938 T, 0.21113 T and 0.35710 T, respectively. Color bright corresponds to high intensity. Because the system has cylindrical symmetry, the major feature in the images is the rings. We observe the bright rings are associated with the special points such as C_1 and C_2, the interference produces some of the weak rings. In all cases, the intensity is high near z-axis because of the magnetic field. When the images in Figure 4 are compared with the detached-electron images of negative ions in an electric field only [1–4,6,7], we find the images in parallel electric and magnetic fields are more complex and interesting.

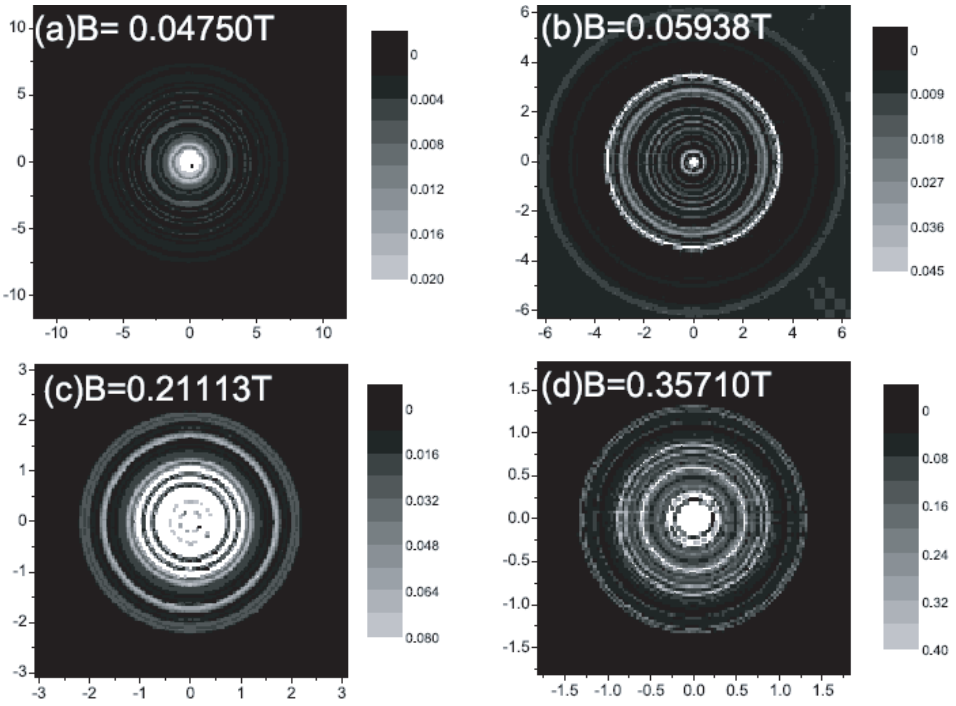

Fig. 4. Detached-electron images on a screen for H^- in parallel electric and magnetic fields. Detached-electron energy, electric field and the position of the screen are the same as in Figure 2 the magnetic field is given in each image.

When comparing the photodetachment of H^- and the results using a point like isotropic source [9–11], we find the detached-electron by a point like source is isotropic, but the angular dependence for detached-electron of H^- is given by equation (13). The angular dependent wavefunction appears as the initial outgoing wave on the surface of the sphere in the semi-classical method described in Section 3. The detached-electron wave amplitude reaching the screen along each orbit is determined by value of the outgoing wavefunction at the emission angle and the amplitude $\tilde{A}$ measuring the wave spreading along the orbit. The angular dependence of the detached-electron leads to more concentration of electron near z-axis and is important in determining the images on the screen.

4 Conclusion

We have studied the spatial distributions of detached-electron in the photodetachment of H^- in parallel electric and magnetic fields taking the existing model for H^- into consideration. We described the bifurcation and anti-bifurcation of detached-electron orbits using $\rho - p_\rho$ diagrams. We obtained uniform semi-classical wave functions for the detached-electron using a mixed position and momentum space method and calculated the flux distributions on a screen. The mixed-space approach makes it more transparent to connect the detached-electron orbits reaching the screen and the structures in the images of detached-electron flux. We found the detached-electron images on the screen consist of strong and weak rings. The strong rings correspond to the special points in the $\rho - p_\rho$ diagrams where bifurcation and anti-bifurcation of orbits occur, and the weak rings correspond to fringes and are consequences of interference of detached-electron traveling along different orbits from the negative ion to the screen. We have shown the interference produces broad fringes with high contrast and narrow fringes with low contrast as in Figure 3. The ring patterns in the detached-electron images can be modified by adjusting the magnetic field strength. The observations of these images will provide direct evidence for bifurcation and anti-bifurcation of detached-electron orbits in parallel electric and magnetic fields.

A paper published very recently by Bracher, Kramer and Delos [10] studied the electron dynamics in parallel electric and magnetic fields. The photodetached-electron was model by an isotropic point source. An isotropic source does not give the correct angular dependence of detached-electron and the detached-electron images on the screen for H^-. However, the study by Bracher, Kramer and Delos [10] using coordinate space should provide similar information regarding the bifurcations of orbits as our method using $\rho - p_\rho$ diagrams, although the perspectives of the two approaches are different.

This research has been supported by NSFC Grant No. 10374061 and No. 90403028. We thank the referee for some useful suggestions.

References

1. C. Blondel, C. Delsart, F. Dulieu, Phys. Rev. Lett. **77**, 3755 (1996)
2. C. Blondel, C. Delsart, F. Goldfarb, J. Phys. B **34**, L281 (2001)
3. C. Blondel, C. Delsart, C. Valli, S. Yiou, M.R. Godefroid, S. Van Eck, Phys. Rev. A **64**, 052504 (2001)

4. C. Delsart, F. Goldfarb, C. Blondel, Phys. Rev. Lett. **89**, 183002 (2002)
5. F. Goldfarb, C. Drag, W. Chaibi, S. Kröger, C. Blondel, C. Delsart, J. Chem. Phys. **122**, 014308 (2005); C. Blondel, W. Chaibi, C. Delsart, C. Drag, F. Goldfarb, S. Kröger, Eur. Phys. J. D **33**, 335 (2005)
6. M.L. Du, Phys. Rev. A **40**, 4983 (1989); I.I. Fabrikant, J. Phys. B **23**, 1139 (1990)
7. G.C. Yang, M.L. Du, Commun. Theor. Phys. **33**, 1 (2000)
8. M.L. Du, Phys. Rev. A **40**, 1330 (1989); J.N. Yukich, T. Kramer, C. Bracher, Phys. Rev. A **68**, 033412 (2003)
9. T. Kramer, C. Bracher, M. Kleber, Europhys. Lett. **56**, 471 (2001)
10. C. Bracher, T. Kramer, J.B. Delos, Phys. Rev. A **73**, 062114 (2006)
11. C. Bracher, J.B. Delos, Phys. Rev. Lett. **96**, 100404 (2006)
12. C. Bracher, T. Kramer, M. Kleber, Phys. Rev. A **67**, 043601 (2003)
13. M.L. Du, J.B. Delos, Phys. Rev. Lett. **58**, 1731 (1987)
14. M.L. Du, J.B. Delos, Phys. Rev. A **38**, 1896 (1988); M.L. Du, J.B. Delos, Phys. Rev. A **38**, 1913 (1988)
15. V.D. Kondratovich, V.N. Ostrovsky, J. Phys. B **23**, 21 (1990); V.D. Kondratovich, V.N. Ostrovsky, J. Phys. B **23**, 3785 (1990)
16. M. Courtney, N. Spellmeyer, H. Jiao, D. Kleppner, Phys. Rev. A **51**, 3604 (1995)
17. A.D. Peters, C. Jaffé, J.B. Delos, Phys. Rev. A **56**, 331 (1997); A.D. Peters, C. Jaffé, J.B. Delos, Phys. Rev. Lett. **73**, 2825 (1997); A.D. Peters, C. Jaffé, J. Gao, J.B. Delos, Phys. Rev. A **56**, 345 (1997)
18. T. Bartsch, J. Main, G. Wunner, J. Phys. A **32**, 3013 (1999)
19. J.M. Mao, J.B. Delos, Phys. Rev. A **45**, 1746 (1992)
20. J.B. Delos, Adv. Chem. Phys. **55**, 161 (1986)
21. M.L. Du, J.B. Delos, Phys. Rev. A **38**, 5609 (1988)